International Journal of Hydrogen Energy 204 (2026) 153326

Contents lists available at ScienceDirect

International Journal of Hydrogen Energy

journal homepage: www.elsevier.com/locate/he

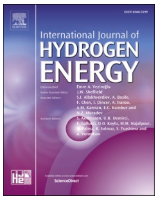

Calcination temperature of the perovskite parent compound controls active metal exsolution and catalytic performance for ethanol steam reforming

Fernando Piazzolla [a], Emerson L. dos Santos Veiga [a], Rafael A. Vicente [b],
Wei-Ling Huang [c], Shan Jiang [c], Pablo S. Fernández [b], Jeffrey T. Miller [c], Fabio C. Fonseca [a],*

[a] *Energy and Nuclear Research Institute (IPEN-CNEN), 05508-000, São Paulo, SP, Brazil*
[b] *Center for Innovation on New Energies and Chemistry Institute, University of Campinas (UNICAMP), Campinas, 13083-852, SP, Brazil*
[c] *Davidson School of Chemical Engineering, Purdue University, 480 Stadium Mall Drive, West Lafayette, IN, 47907-2100, USA*

ARTICLE INFO

Keywords:
Hydrogen production
Ethanol steam reforming
Exsolution
Nickel catalyst
Perovskite
Calcination temperature

ABSTRACT

The imperative need for sustainable hydrogen (H_2) production has driven increasing research into efficient ethanol steam reforming (ESR) catalysts. This study demonstrates that the calcination temperature of $La_{0.4}Sr_{0.4}Ti_{0.8}Ni_{0.2}O_{3-\delta}$ (LSTN) controls surface area, directly influencing both the nickel reducibility and the formation of exsolved Ni^0 nanoparticles (5–15 nm). Such parameters result in microstructural properties determining the catalytic performance. ESR catalytic tests at 600 °C, showed that samples calcined at lower temperature (650 °C) achieved complete ethanol conversion and stable H_2 yield (4.04 mol $mol^{-1}_{ethanol}$), whereas increasing calcination temperatures (800 and 1200 °C) significantly reduced surface area and altered product distribution, favoring ethanol dehydrogenation over reforming. The robust properties of exsolved catalysts were demonstrated by ESR stability test that revealed sustained H_2 production despite partial deactivation. The experimental results evidenced that controlling the calcination temperature of the parent LSTN oxide before exsolution is a practical parameter for tuning Ni exsolution and catalytic performance, to establish LSTN as a highly effective and stable material for renewable H_2 production via ESR.

1. Introduction

Global energy demands and the environmental impacts of fossil fuels have intensified the search for sustainable alternatives. Renewable sources like solar, wind, and biomass are essential for reducing greenhouse gas emissions and improving energy security [1,2]. Among these solutions, hydrogen (H_2) has gained attention as a clean energy carrier due to its high energy density and potential for sustainable production [3,4]. Ethanol steam reforming (ESR) stands out in this context, utilizing biomass-derived ethanol to efficiently generate H_2. Unlike natural gas reforming, ESR reduces reliance on fossil fuels and aligns with global energy transition policies, highlighting biofuels as key contributors to a sustainable energy future [5,6].

However, ESR remains limited by catalyst durability and efficiency. Noble metals such as platinum (Pt) and rhodium (Rh) are traditionally favored for their high activity and resistance to deactivation. However, their scarcity and cost have shifted focus to non-noble alternatives, particularly nickel (Ni)-based catalysts, which are widely studied for their affordability. Nevertheless, Ni-based catalysts face stability challenges due to carbon deposition and sintering that block the active sites and reduce the catalyst surface area, respectively. To overcome such deactivation mechanisms, strategies like the addition of promoters (e.g., lanthanum, cerium), advancing metal-support interaction (e.g., mixed oxides), or improving metal dispersion can improve catalyst durability. These innovations highlight the potential of optimized non-noble catalysts as sustainable solutions for H_2 production via ESR [7–12].

By combining a highly dispersed metal and tailored supports, a promising strategy to enhance the catalytic properties of oxide materials is the exsolution of metal nanoparticles (NPs) [13–15]. The exsolution process involves first incorporating metal cations into the crystal lattice of a host oxide matrix, typically a perovskite such as lanthanum doped strontium titanate (La–$SrTiO_3$, LST), to create a solid solution. Subsequently, under a reducing atmosphere, these cations exsolve to the surface as socketed NPs [16].

While LST-based compounds exhibit excellent chemical stability, their catalytic activity remains inferior to traditional ceramic-metal

---

* Corresponding author.
E-mail address: fabiocf@usp.br (F.C. Fonseca).

https://doi.org/10.1016/j.ijhydene.2025.153326
Received 22 October 2025; Received in revised form 4 December 2025; Accepted 29 December 2025

composites used in ethanol steam reforming (ESR). To address this limitation, doping LST with Ni and subsequently exsolving Ni^0 NPs offers a pathway to achieving materials with high catalytic activity. The exsolution process ensures uniform distribution of metallic NPs on the ceramic surface with strong metal-support interaction, which enhance stability and performance [13,17].

Factors that influence exsolution include A-site non-stoichiometry, B-site dopants, crystal orientation and strain, as well as extrinsic variables such as oxygen partial pressure, humidity, temperature and treatment time [18,19]. Controlling grain size and surface area of the oxide matrix offers a complementary strategy to tune nanoparticle exsolution and properties [19].

A prior study [20] using $La_{0.4}Sr_{0.4}Ti_{0.8}Ni_{0.2}O_{3-\delta}$ (LSTN) demonstrated the dependence of both time and temperature of the thermochemical treatment on Ni^0 nanoparticle exsolution. Changing such parameters was directly reflected in the catalytic activity towards ESR. The temperature for the reducing treatment enabled controlling the metallic nanoparticle size, while increasing the duration of the reducing treatment promoted a higher surface density of the exsolved metallic particles. This previous study successfully generated active metallic Ni in LST and paved the way for further optimization to improve catalytic performance.

The present study focuses on the less-explored dependence of the processing parameters of the parent compound that precedes the reduction treatment for exsolution. It is demonstrated that the calcination temperature and the resulting microstructural properties of the LSTN host matrix exert a strong influence on catalytic performance. The detailed characterization highlights the key role of controlling processing parameters in achieving high-performance catalysts with exsolved nanoparticles for H_2 production via ESR.

2. Experimental

2.1. Synthesis

The nominal composition investigated was $La_{0.4}Sr_{0.4}Ti_{0.8}Ni_{0.2}O_{3-\delta}$ (lanthanum- and nickel-doped strontium titanate). The compound was synthesized via the Pechini method as demonstrated previously [20]. Initially, citric acid ($C_6H_8O_7$, 99.5 %, Vetec) was dissolved in distilled water. Sequentially, nickel nitrate ($Ni(NO_3)_2 \cdot 6H_2O$, 99 %, Sigma-Aldrich), lanthanum nitrate ($La(NO_3)_3 \cdot 6H_2O$, 99.999 %, Sigma-Aldrich), strontium nitrate ($Sr(NO_3)_2$, 99.0 %, Sigma-Aldrich), and titanium isopropoxide ($C_{12}H_{28}O_4Ti$, 97 %, Aldrich) dissolved in ethylene glycol ($C_2H_6O_2$, 99 %, Sigma-Aldrich) were added. The molar ratio of citric acid to metal cations was maintained at 1:2, while the mass ratio of citric acid to ethylene glycol was 60:40. Components were mixed in a PTFE reactor at 60 °C with reagents added every 30 min. After the last addition, the solution was stirred for 1 h and then dried at 180 °C until solvent removal. The dried material was thermally treated at 250 °C for 3 h under static air with a heating ramp of 10 °C min^{-1} to dehydrate the resin. The resulting powder was homogenized using an agate mortar.

To investigate the influence of calcination temperature on the formation of nanoparticle, samples were calcined at 650 °C, 800 °C, and 1200 °C under static air. The heating rate was 10 °C min^{-1}, and the calcination time at targeted temperature was 4 h. Throughout this work, different batches of the studied compounds were synthesized with excellent reproducibility.

The thermochemical treatment for exsolution of the single-phase oxides was carried out in a tubular furnace at 900 °C for 20 h under a continuous flow of pure H_2 (99.9999 %). Thermal cycling, including both heating and cooling, occurred at a controlled rate of 10 °C min^{-1} under pure H_2.

2.2. Chemical and structural characterization

X-ray diffraction (XRD) analysis was performed using a Rigaku SMARTLAB II diffractometer with Cu K_α radiation ($\lambda = 1.5406$ Å) in Bragg-Brentano geometry. Data were collected in the 2θ range of 20°–90° with a step size of 0.05° and a scan rate of 5° min^{-1}. The lattice parameter (a) was determined from indexed XRD peaks using Bragg's law, $d_{hkl} = \frac{\lambda}{2 \sin \Theta}$; $\lambda_{Cu\ K\alpha} = 1.5406$ Å) and the cubic relation $a_{hkl} = d_{hkl} \cdot \sqrt{h^2 + k^2 + l^2}$. The final a corresponds to the weighted average of all a_{hkl} values. The error was estimated as the standard deviation. The average crystallite size was calculated using the width of the diffraction peaks according to the Scherrer equation.

Wavelength dispersive X-ray fluorescence (WDXRF) spectroscopy was conducted on a Rigaku Supermini200 spectrometer equipped with a palladium X-ray source ($\lambda = 0.585$ Å, Kα). Samples were analyzed in powder form using a semi-quantitative method.

Temperature-programmed reduction (TPR) analyses were conducted to assess the reducibility of the samples and the temperature ranges of reduction. Experiments were carried out on a Quantachrome ChemBET Pulsar TPR/TPD system. Approximately 100 mg of sample was heated from room temperature to 1000 °C under a 10 % H_2/N_2 flow (30 mL min^{-1}) at 10 °C min^{-1}. Hydrogen consumption was monitored via a thermal conductivity detector (TCD) and estimated using a CuO reference sample.

Specific surface area was determined by the Brunauer–Emmett–-Teller (BET) method using nitrogen adsorption–desorption isotherms (Micromeritics ASAP 2020), after degassing the samples under a nitrogen flow at 200 °C for 2 h.

The morphological features and particle dimensions of the catalysts were characterized using field-emission gun scanning electron microscopy (FE-SEM) on a JEOL JSM-IT700HR instrument. Accelerating voltages of 3–6 kV were applied during imaging. Particle size distributions were quantified by analyzing diameters extracted from FE-SEM micrographs using ImageJ® software, with more than 100 particles measured for each sample, allowing calculation of the corresponding average diameter and standard deviation. For nanoscale structural analysis, high-resolution transmission electron microscopy (HR-TEM) and energy-dispersive X-ray spectroscopy (EDS) were carried out using a Talos F200X G2 microscope.

X-ray Photoelectron Spectroscopy (XPS) measurements were conducted at the Brazilian Nanotechnology National Laboratory (LNNano/CNPEM) in Campinas, Brazil. Spectra were acquired using a Thermo Scientific K-Alpha spectrometer with a monochromatic Al Kα X-ray source (1486.6 eV). Data were collected in the binding energy range of 100–1500 eV. All spectra were energy-referenced to the C 1s peak at 284.6 eV and processed using CASA XPS software.

X-ray Absorption Spectroscopy (XAS) was performed at the 8-ID ISS beamline at the NSLS-II synchrotron light source. XAS spectra were obtained at the Ni K edge, with a varying energy step (5 eV before the edge, 0.2 eV at the edge, and a variable step from 0.2 to 5 eV after the edge depending on the k value). The spectra were collected under pure He atmosphere at room temperature to avoid thermal disorder. Data fitting was carried out using WinXAS software. X-ray Absorption Near-Edge Structure (XANES) spectra were normalized by applying a linear fit to the pre-edge region and a second-order polynomial after the edge. To enhance the signal-to-noise ratio, we collected between 5 and 25 spectra for each analysis, depending on the noise level for each sample. For the Extended X-ray Absorption Fine Structure (EXAFS) analysis, the first-shell contributions were fitted in the k^2-weighted Fourier transform of the data over the k-range of 2.3–12 $Å^{-1}$. The samples consisted of quartz capillary tubes sealed by Kapton wool and filled with the perovskite powder under controlled atmosphere for the exsolution in different conditions. All samples were exposed to an *in-situ* two-step thermal treatment: firstly, samples were heated to 200 °C under 20 % He and 80 % O_2, then they were heated to 600 °C in 10 % H_2 and 90 %

He. The heating was performed using ramps of 13.5 °C min^{-1}.

Thermogravimetric analysis (TG) was carried out on a Setaram LabSys instrument heating from room temperature to 1000 °C at a rate of 10 °C min^{-1} under synthetic air (50 mL min^{-1}, 99.9992 % purity).

Raman spectroscopy was conducted using a Horiba Jobin Yvon XploRA-PLUS system with a 532 nm laser, a 50x objective lens, and a spectral range of 200–1200 cm^{-1}.

2.3. *Catalytic testing: ethanol steam reforming*

Catalytic tests were conducted in a fixed-bed quartz U-tube reactor (6 mm inner diameter) loaded with 20 mg of catalyst, the catalyst was positioned and retained in the reactor with glass-wool plugs, operating at near ambient pressure (~1 bar). After assembling the fixed-bed reactor and prior to all reactions, the catalyst was reduced under pure H_2 (30 mL min^{-1}) at 600 °C for 1 h, followed by purging with N_2 (30 mL min^{-1}) for 10 min at the same temperature to remove residual hydrogen.

The ESR reaction was carried out at 600 °C using a 3:1 M ratio of H_2O:Ethanol to promote the water-gas shift reaction. Ethanol and water vapors were generated using separate liquid saturators and introduced into the reactor via two separate N_2 streams (30 mL min^{-1} each), with the saturators maintained at 20 °C (ethanol) and 60 °C (water) to control vapor partial pressures and ensure reproducible vapor compositions. Catalytic activity is reported as the ratio W/F defined as the catalyst mass (20 mg) divided by the total volumetric flow rate of reagents. The flow rate was calculated based on the saturator vapor pressure at 20 °C and a 60 mL min^{-1} of N_2 carrier flow. Effluent gases were analyzed using an Agilent 7890A gas chromatograph equipped with a molecular sieve column, a Plot U column, a flame ionization detector (FID), and a thermal conductivity detector (TCD).

All catalytic experiments were conducted in at least duplicate using independently synthesized catalyst batches. Blank tests were performed without catalyst by measuring the ethanol and water vapor concentrations five consecutive times under identical inlet-flow conditions. The averaged blank values were used for calculating conversions and product yields, and no gaseous reaction products were detected in the blank condition.

Ethanol conversion (X_{ethanol}) and product distribution (P_x) were calculated as [21]:

$$\chi_{ethanol} = \frac{((n_{ethanol})\,fed\,/(n_{ethanol})exit)}{n_{ethanol}} \cdot 100 \tag{1}$$

$$P_x = \frac{(n_x)produced}{(n_{total})produced} \cdot 100 \tag{2}$$

where n_x is the moles of product x, and n_{total} products excludes water.

The selectivity (s_i) of the catalysts for the respective products and the H_2 yield (y_{H_2}) were determined according to Equations (3) and (4):

$$s_i(\%) = \frac{n_i \times v_i}{2 \times n_{ethanol}} \cdot 100 \tag{3}$$

$$y_{H_2} = \frac{n_{H_2}}{n_{\ ethanol}} \tag{4}$$

where n_i is the molar amount of product *i*, v_i denotes the number of carbon atoms in the carbon-containing product species, $n_{ethanol}$ represents the molar quantity of converted ethanol and n_{H_2} is the molar amount of H_2 produced, all defined according to the stoichiometry of the ESR reaction.

3. Results

3.1. *Effect of calcination temperature*

Samples calcined at different temperatures were analyzed by XRD, and the corresponding diffraction patterns are presented in Fig. 1a. The selected calcination temperature range was defined by thermogravimetric analysis of the polymeric precursor of the oxide phase (see Fig. 1S) and represents typical processing temperatures for perovskite produced by chemical methods. Specifically, 650 °C is the lowest firing temperature to ensure complete burnout of organics resulting in single-phase compound. Thus, varying the calcination temperature of the parent compound from 650 to 1200 °C covers a relatively broad processing temperature range for oxides, spanning from low-temperature crystallization to high-temperature regimes, which are particularly useful for understanding how exsolution behaves in densified perovskite structures. For all calcination temperatures, single-phase materials were obtained, with no noticeable peak shift compared to the reference phase La-doped $SrTiO_3$ ($La_{0.4}Sr_{0.4}TiO_{3\text{-}\delta}$, LST) synthesized by the same method and fired at 650 °C for comparison. XRD patterns showed single-phase materials at all calcination temperatures. The lattice parameter was 3.911 ± 0.02 Å for LST and 3.911 ± 0.004 Å, 3.910 ± 0.003 Å and 3.911 ± 0.004 Å for LSTN 650, LSTN 800 and LSTN 1200, respectively, confirming cubic-phase stability. Regarding the microstructure, the estimated crystallite sizes were 15 ± 1 nm (LST), 13 ± 1 nm (LSTN 650), 15 ± 1 nm (LSTN 800), and 18 ± 2 nm (LSTN 1200).

The nominal composition for $La_{0.4}Sr_{0.4}Ti_{0.8}Ni_{0.2}O_{3\text{-}\delta}$ (excluding oxygen) corresponds to mass percentages of La = 39.50 %, Sr = 24.92 %, Ti = 27.22 %, and Ni = 8.35 %, as calculated from the theoretical chemical formula. Semiquantitative Wavelength-dispersive X-ray spectroscopy (WDXRF) analysis revealed deviations from the nominal values, indicating a relative excess of A-site cations (La + Sr), a deficiency in Ti content, and an excess of Ni. Based on experimental WDX data, the synthesized material can be approximated by the formula $La_{0.50}Sr_{0.55}Ti_{0.75}Ni_{0.25}O_{3\text{-}\delta}$. Within the accuracy limits of the technique, these deviations remain within acceptable ranges compared to the nominal composition.

To determine the optimal reduction temperature for nickel exsolution (Ni^0), H_2-TPR analysis was performed. The reduction profiles are shown in Fig. 1b. The LST 650 sample, without Ni, exhibits a broad reduction peak with maximum at ~720 °C, ascribed to the oxygen loss of the perovskite phase. In the Ni-substituted samples (LSTN), the hydrogen consumption peaks shift to higher temperatures as the calcination temperature increases. For LSTN 650, a broad peak develops between ~300 °C and ~600 °C, with a shoulder at ~390 °C and a maximum at ~500 °C that are assigned to surface and bulk nickel reduction [22,23], and a less pronounced peak at ~720 °C that is likely related to perovskite lattice oxygen release. The estimated total H_2 consumption for the LSTN 650 sample was significantly higher than that of LST 650 (175 ± 15 μmol g^{-1} versus 4 ± 0.5 μmol g^{-1}).

For the LSTN 800 sample, two reduction events were observed at ~425 °C and ~545 °C, both attributed to nickel reduction. The shift to higher reduction temperatures relative to LSTN 650 likely reflects microstructural changes induced by the higher calcination temperature, which hinder nickel reducibility (e.g., grain growth and decreased surface area). No high-temperature events attributable to lattice oxygen release were detected within the experimental temperature range. The total H_2 consumption for LSTN 800 (200 ± 20 μmol H_2 g^{-1}) was marginally higher than that of LSTN 650. By contrast, the LSTN 1200 sample exhibited two less pronounced, but separated peaks at ~495 °C and ~760 °C, possibly attributed to nickel reduction. The higher peak temperatures are consistent with sintered grains and a lower specific surface area of the LSTN 1200, which shift reduction to higher temperatures. This effect is reflected in the substantially lower total H_2 consumption for LSTN 1200 (64 ± 6 μmol H_2 g^{-1}) compared with samples calcined at lower temperatures.

Based on the theoretical consumption for complete Ni^{2+} reduction, the experimental H_2 uptake corresponds to a reduction degree of approximately 16 % for LSTN 650, 19 % for LSTN 800, and 6 % for LSTN 1200. However, an accurate quantification of Ni exsolution solely from TPR data is challenging due to the dynamic of the heating temperature

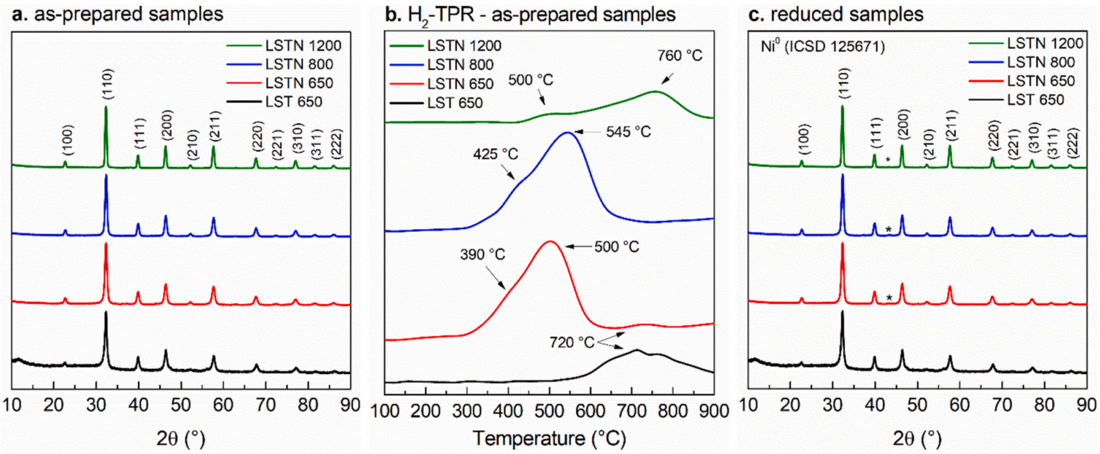

Fig. 1. (a) XRD patterns of the as-synthesized samples (as-prepared) calcined at different temperatures. (b) H_2-TPR profiles for the samples before and after reduction. (c) XRD patterns of the samples after reduction treatment at 900 °C for 20 h.

ramp, which differs from the isothermal conditions typically used for catalyst activation. Therefore, subsequent analyses were performed on samples reduced at a fixed temperature to better understand the material state under reaction conditions.

Based on the H_2-TPR results, a reduction temperature of 900 °C was selected to ensure nickel nanoparticle exsolution while favoring complete reduction of both surface and bulk species. This temperature was standardized for all samples. The XRD of all reduced samples exhibited the characteristic peak for Ni^0 at 2θ ~43° [24], as shown in Fig. 1c. Negligible differences were observed in the estimated lattice parameters of the samples after reduction (<0.005 Å).

A progressive decrease in the BET surface area of the as-prepared samples was observed with increasing calcination temperature, from 40 ± 3 $m^2\ g^{-1}$ (LSTN 650) to 24 ± 3 $m^2\ g^{-1}$ (LSTN 800), and finally to 4.3 ± 0.9 $m^2\ g^{-1}$ (LSTN 1200). This trend is directly related to the reduced reducibility of Ni, in agreement with the TPR results. The loss of surface area due to particle coarsening strongly correlates with the shift of bulk nickel reduction to higher temperatures and the observed decrease in H_2 consumption. Following reduction at 900 °C for 20 h, the surface areas of LSTN 650 and LSTN 800 decreased significantly to 21 ± 1 $m^2\ g^{-1}$ and 14 ± 1 $m^2\ g^{-1}$, respectively. This decrease was expected, as the temperature of the reducing thermal treatment (900 °C) exceeded their initial calcination temperatures. Nevertheless, LSTN 650 maintained the highest surface area, whereas that of LSTN 1200 further decreased to 2.8 ± 0.7 $m^2\ g^{-1}$.

These results provide a comprehensive link between microstructure and reducibility. The severe sintering in LSTN 1200, evidenced by its low surface area and larger crystallite size (~18 nm vs. 13–15 nm for lower-temperature samples), limits hydrogen diffusion and surface accessibility. This constraint explains the suppressed reducibility (~6 %) observed in the TPR profiles, demonstrating that the extent of nickel exsolution is critically limited by the host's sintered microstructure.

The observed changes in surface area and microstructure are expected to influence the chemical states and surface composition of the materials, which can be probed by XPS and XAS. Accordingly, the XPS spectra of the O 1s region for the as-prepared and reduced samples are presented in Fig. 2. For LSTN 650 (Fig. 2a), the spectrum is deconvoluted into two components: (i) the dominant peak at ~529 eV, assigned to lattice oxygen O^{2-} of the metal oxides (O_{MO}) within the perovskite structure, and (ii) a smaller peak at ~531 eV, attributed to adsorbed O^- oxygen species (O_{ads}) such as hydroxyls, carbonates, or carbonyl groups, for example [24,25]. The larger area of the O_{MO} peak confirms that structural oxygen predominates at the surface.

Following spectral deconvolution, the intensity ratio $r = O_{ads}/O_{MO}$ was calculated. For LSTN 650, this ratio decreased from 0.63 (as-prepared) to 0.37 (reduced), indicating the preferential removal of adsorbed surface species during H_2 treatment. A similar trend was observed for LSTN 800 (Fig. 2b), where r decreased from 0.74 to 0.36. In contrast, the variation in r for LSTN 1200 was much less pronounced, which is consistent with the limited reducibility observed in the TPR data.

The observed changes in surface oxygen species suggest a modification in surface stoichiometry, likely associated with the creation of oxygen vacancies. Surface oxygen vacancies in perovskites serve as nucleation sites for Ni exsolution, yielding small, strongly anchored and

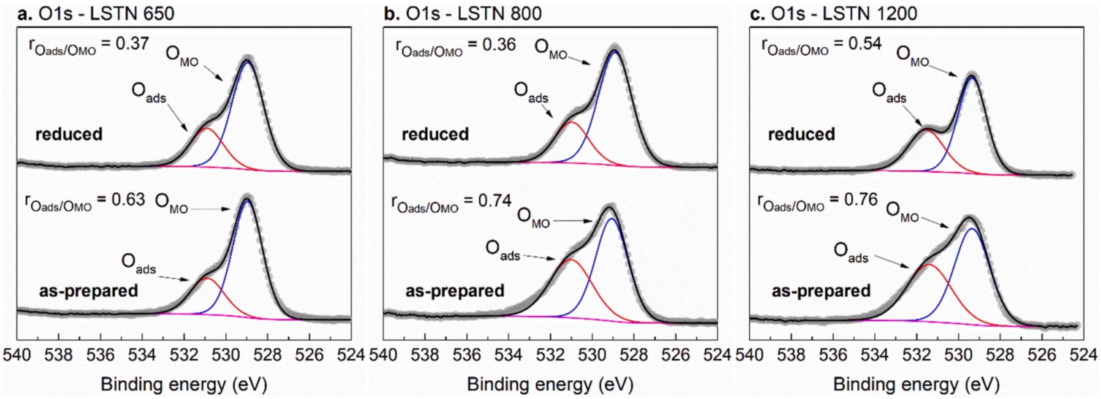

Fig. 2. O 1s XPS spectra for the as-prepared and reduced samples: (a) LSTN 650, (b) LSTN 800, and (c) LSTN 1200. The ratio between adsorbed oxygen species (O_{ads}) and metal oxide lattice oxygen (O_{MO}) is displayed for each sample before and after reduction treatment.

uniformly distributed Ni^0 nanoparticles. Higher vacancy concentration increases reducibility and accelerates exsolution kinetics, which ultimately facilitates the formation of highly dispersed metallic sites that enhance catalytic performance [11,26].

X-ray absorption experiments were carried out to further study the exsolution in LSTN compounds. The XANES spectra are shown in Fig. 3a–d. All samples show mostly Ni^{2+} behavior, with well-defined pre-edge peak 8.3333 keV, characteristic of Ni^{2+} ions [27], and the main peak at 8.3466 keV. By reducing Ni during the exsolution step, the Ni^0 XANES edge overlaps the Ni^{2+} pre-edge peak. Moreover, there is a drop in the white line in the edge as Ni^{2+} is reduced. We observe that the sample calcined at 650 °C is the only sample which forms the Ni^0 shoulder after the reduction at 600 °C.

The EXAFS profiles (Fig. 3e–g) show the conversion from Ni^{2+} where there are Ni–O and Ni–*O*–Ni bonds to Ni^0 and the formation of Ni–Ni bonds. After reduction, Ni–Ni bonds appear, due to the formation of metallic Ni during exsolution. These bonds are highlighted in the EXAFS profiles of the reference samples (Fig. 3h). Both the XANES and EXAFS show that only the sample calcined at 650 °C forms metallic Ni after reduction at 600 °C, whereas the other two samples remain mostly in the

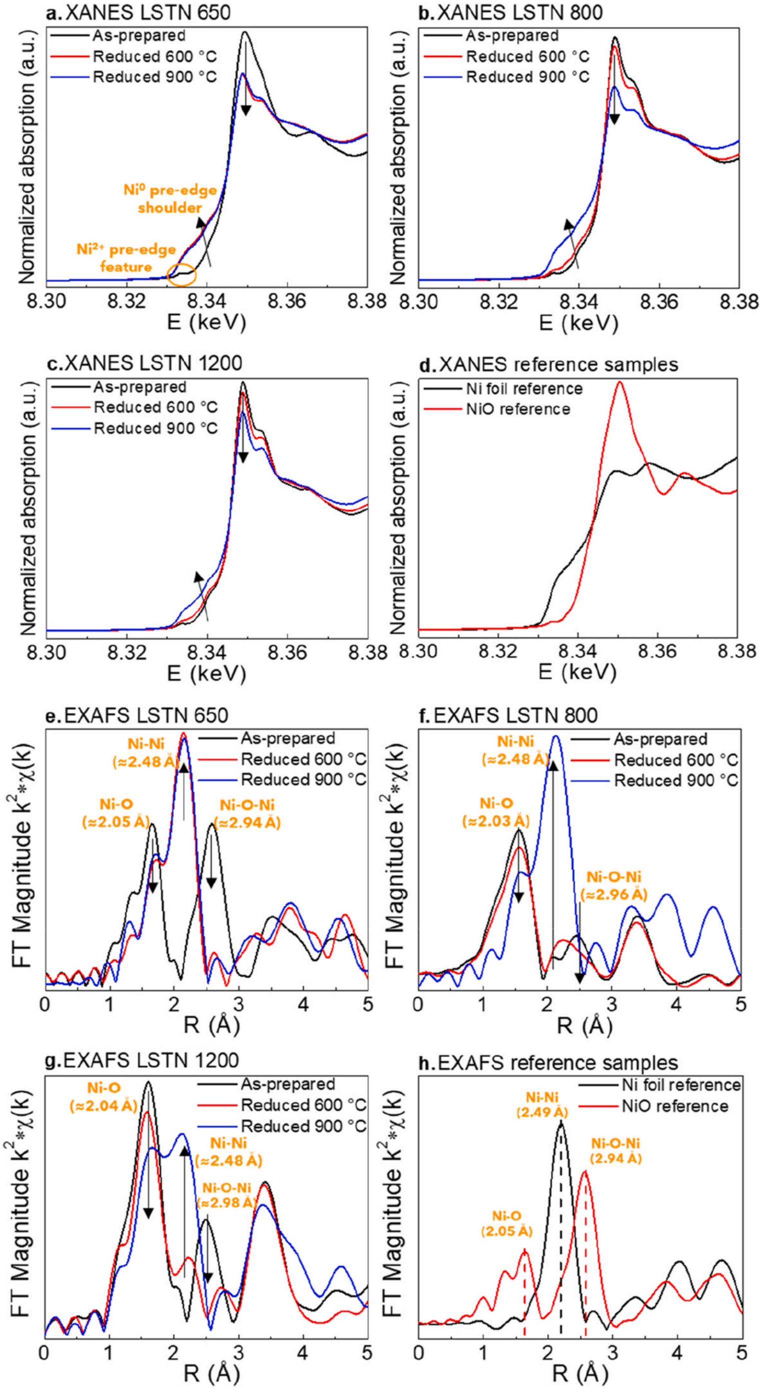

Fig. 3. XANES spectra for: (a) LSTN 650, (b) LSTN 800, (c) LSTN 1200, (d) Ni foil and NiO reference samples. The changes with Ni reduction are highlighted by the arrows. The pre-edge feature and pre-edge shoulder are shown. EXAFS uncorrected for phase-shift profiles for: (e) LSTN 650, (f) LSTN 800, (g) LSTN 1200, (h) Ni foil and NiO reference samples. The Ni–O, Ni–Ni, and Ni–*O*–Ni bonds and their corrected bond distances are highlighted. Some EXAFS peaks are normalized to facilitate visual comparison.

LSTN phase. The extracted coordination numbers and data fitting parameters are shown in Table S1.

The expected CN for Ni inserted into the perovskite lattice is 6 for both the Ni–O bond and Ni–*O*–Ni bond, since Ni atoms occupy octahedral sites bound to 6 oxygens atoms, and each octahedron is connected to another 6 octahedra. On the other hand, the CN for Ni–*O*–Ni in NiO is 12 owing to its rock-salt structure (ICSD 76669). It was observed that samples show the expected CNs ≤6 (Table S1) for Ni–*O*–Ni characteristic of Ni^{2+} atoms in the perovskite lattice for all calcination temperatures of the as-prepared samples. After reduction, there is a remaining Ni^{2+} contribution (almost all reduced samples show approximately a 50:50 Ni^{2+}/Ni^0 fraction), which can be related to an incomplete reduction of bulk.

When analyzing the effect of calcination temperature, XAS shows that lower temperatures lead to easier Ni reducibility in accordance with the H_2-TPR data. While for LSTN 650, Ni starts forming during reduction at 650 °C, for LSTN 800 major Ni^0 contribution develops at 900 °C, whereas for LSTN 1200 there is a lower metallic Ni fraction at 900 °C. Additionally, as the calcination temperature increases, the Ni–*O*–Ni coordination number decreases considerably, even though the Ni–O remains close to 6. This could indicate that the high calcination temperature has a weak effect on the NiO_6 sites, but it strongly disrupts the NiO_6 network, which likely impacts the diffusion of Ni atoms necessary for exsolution.

The FE-SEM micrographs in Fig. 4 highlight the microstructural differences induced by the distinct calcination temperatures. In the as-prepared LSTN 650 sample (Fig. 4a, left panel), a relatively regular surface of the oxide matrix is observed. After reduction, bright Ni^0 NPs with irregular morphology are clearly visible, anchored to the porous oxide matrix. The average diameter of the Ni^0 NPs was estimated at 25 nm, while their surface density (ρ_s) was ~25 NPs μm^{-2}. Similar features were observed for the LSTN 800 sample (Fig. 4b), where, after reduction, Ni^0 NPs with a more spherical morphology became evident. An increase in nanoparticle size with temperature was confirmed, as the average diameter of the Ni^0 particles was estimated at 36 nm. For the LSTN 1200 sample, grain growth was evident in the as-prepared material, consistent with the lower surface area obtained by the BET method. After reduction, Ni^0 NPs were mainly observed at the grain boundaries, with an average diameter of 42 nm. No significant changes in the ρ_s of Ni^0 nanoparticles were observed for the LSTN 800 and LSTN 1200 samples compared to the LSTN 650 sample. Complementary EDS measurements acquired by HR-TEM (Fig. S2) further corroborate the exsolution and confirm the presence of metallic nickel in the analyzed regions.

The combined results showed that the calcination temperature establishes a clear physicochemical gradient across the perovskites, which indicates that the reduction of Ni is progressively hindered by increasing the calcination temperature. LSTN 650 retains the highest BET surface

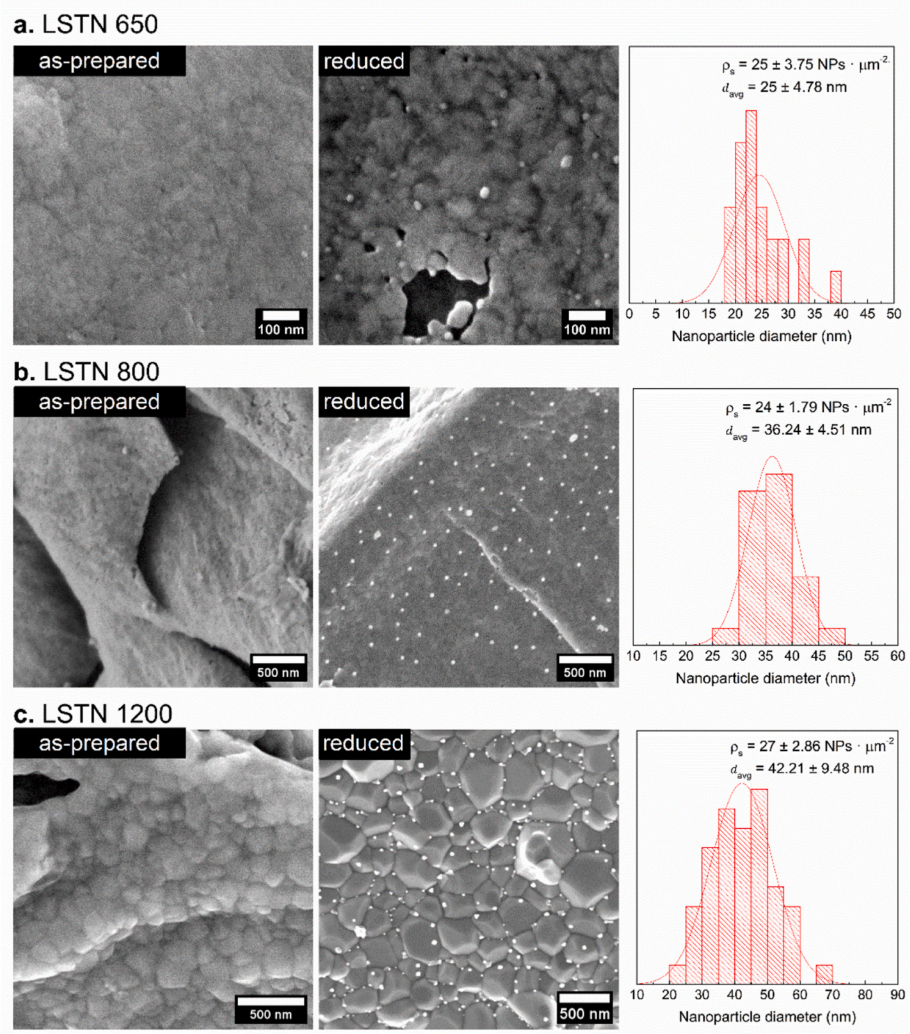

Fig. 4. FE-SEM micrographs of the as-prepared LSTN samples calcined at different temperatures (left panels) and after reduction at 900 °C for 20 h (center panels). The right panels show the histograms of the average Ni^0 NPs diameter and the surface number density (ρ_s).

area. The obtained results for this sample show that Ni can be exsolved as Ni^0 (confirmed by XAS, SEM, and TEM) with sufficient thermal input and exhibits the highest reducibility. By contrast, LSTN 800 exhibits a moderate surface area and its H_2-TPR peaks shift ~30 °C higher. The exsolved Ni^0 NPs remain finely dispersed but are slightly larger (25–50 nm, compared to 15–40 nm of LSTN 650). LSTN 1200 displays the opposite extreme of LSTN 650: its surface area collapses due to sintering, porosity is largely lost, and the reduction of Ni^{2+} occurs at much higher temperatures with drastically reduced H_2 consumption and significant residual Ni^{2+} content (XAS) after reduction. SEM revealed larger perovskite oxide crystals alongside coarse Ni^0 congregating along grain boundaries. Together, these results demonstrate that higher calcination temperatures fundamentally compromise surface area and reducibility kinetics, concentrating Ni^0 at grain boundaries and reducing active site accessibility.

3.2. Catalytic performance

All samples underwent catalytic testing for ethanol steam reforming (ESR) at 600 °C for 20 h, as shown in Fig. 5.

Ethanol conversion and product distribution for the LSTN 650 sample are presented in Fig. 5a. Complete ethanol conversion (100 %) was maintained throughout the ESR test. H_2 and CO production remained stable at ~67 % and 22 %, respectively, over the entire reaction. CO_2 and CH_4 were detected at concentrations of 7.5 % and 3.3 %, respectively, while C_2H_4 had negligible concentration.

The high ethanol conversion, significant H_2 production (yield of 4.04 $\text{mol mol}^{-1}_{\text{ethanol}}$; Table 1), and the presence of CO and CH_4 indicate coexistence of multiple reaction pathways. This H_2 yield corresponds to ~67 % of the theoretical maximum (6 mol H_2 per mol ethanol) for complete steam reforming (Equation (5)). The deviation from equilibrium is primarily due to competing reactions and the partial suppression of the water-gas shift reaction. While partial ethanol reforming (Equation (6)) is dominant, the substantial H_2 yield and 5–10 % CO_2 concentration suggests significant contribution from complete ethanol steam reforming. The low absolute CO_2 level implies that the material's properties and reaction temperature (600 °C) partially suppress the WGS reaction [28,29].

The simultaneous detection of methane and CO may be compatible with thermal decomposition of acetaldehyde at temperatures near 600 °C (Equation (7)) [30–33]. For comparison, an ESR test was performed on the undoped LST and on the as-prepared LSTN 650 sample (Fig. S3). In the as-prepared samples, ethanol conversion gradually decreased during the reaction, stabilizing at ~40 %, which is significantly lower than that of the reduced sample. Ethanol dehydrogenation was the predominant pathway (Equation (8)), yielding acetaldehyde and hydrogen, while ESR and acetaldehyde also occurred. Ethanol dehydrogenation was the main pathway of the undoped sample.

$$C_2H_5OH + 3H_2O \rightarrow 2CO_2 + 6H_2 \ \Delta H^\circ = +173 \text{ kJ / mol} \quad (5)$$

$$C_2H_5OH + H_2O \rightarrow 2CO + 4H_2 \ \Delta H^\circ = +256 \text{ kJ / mol} \quad (6)$$

$$CH_3CHO \rightarrow CH_4 + CO \ \Delta H^\circ = -18 \text{ kJ / mol} \quad (7)$$

$$C_2H_5OH \rightarrow CH_3CHO + H_2 \ \Delta H^\circ = +68 \text{ kJ / mol} \quad (8)$$

The LSTN 800 sample exhibits a distinct ethanol conversion and product distribution as compared to LSTN 650 (Fig. 5b). The LSTN 800 catalyst undergoes partial deactivation during the initial 3 h of ESR reaction, observed as a decay in ethanol conversion and increased fraction of acetaldehyde. The deactivation is probably associated with coke accumulation. Following initial deactivation, ethanol conversion stabilized at ~68 % over the remaining reaction time. Product distribution included: H_2 (47 %; yield of 1.17 $\text{mol mol}^{-1}_{\text{ethanol}}$), acetaldehyde (~30 %), CO (15 %), and CO_2 and CH_4 (>5 %) after 20 h of ESR. This H_2

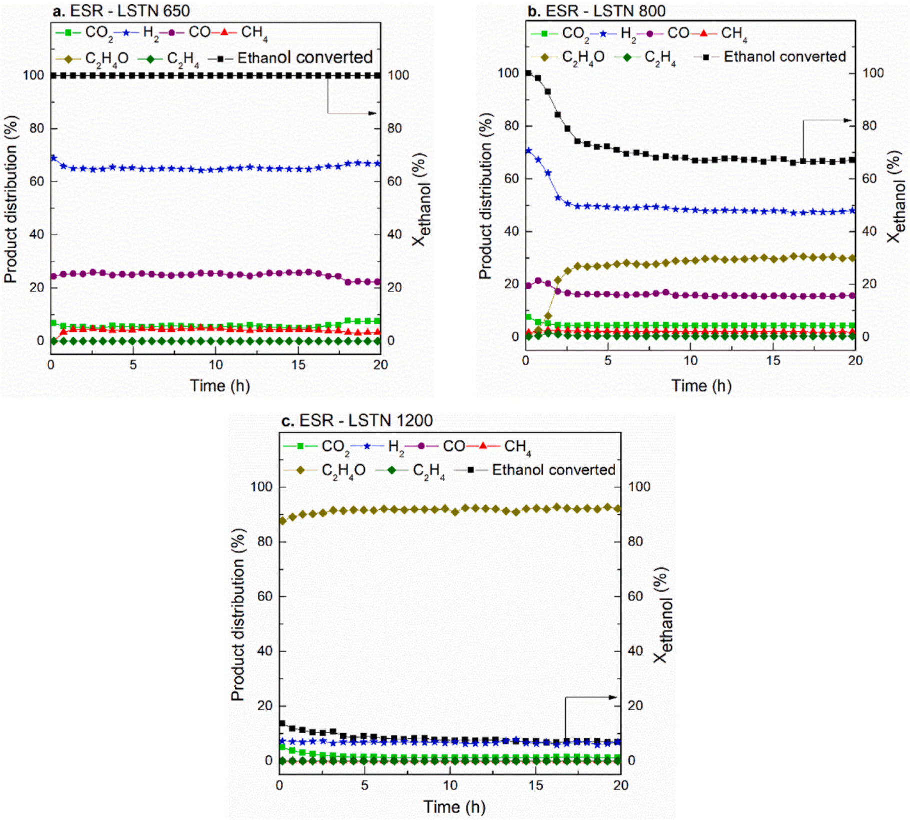

Fig. 5. Product distributions and ethanol conversion ($X_{ethanol}$) during ESR tests over the (a) LSTN 650, (b) LSTN 800, and (c) LSTN 1200 samples at 600 °C for 20 h (Catalyst mass = 20 mg; W/F = 0.020 g s mL^{-1}).

Table 1
– Ethanol conversion, H_2 yield, and carbon accumulation on spent catalysts after ESR under different reaction conditions.

Samples	ESR reaction duration (h)	ESR reaction temperature (°C)	Ethanol conversion (%)	H_2 yield (mol·mol $^{-1}_{ethanol}$)	Carbon formed (mgC g_{cat}^{-1}·h^{-1})
LSTN 650	20	600	100 ± 0	4.04 ± 0.05	7.37 ± 0.37
LSTN 800	20	600	68 ± 2	1.17 ± 0.10	25.2 ± 1.3
LSTN 1200	20	600	7.8 ± 0.7	0.07 ± 0.04	0.42 ± 0.04
LSTN 650	85	500	40 ± 2	1.10 ± 0.12	13.30 ± 0.67

yield represents about 19 % of the theoretical maximum, indicating a significant deviation from equilibrium. The decreased specific surface area (relative to LSTN 650) impairs ethanol and water-steam adsorption and alters Ni^0 nanoparticle size and dispersion, resulting in larger metallic particles that are more prone to coking [34]. Carbonaceous deposits then accumulate and block access to the Ni^0 sites responsible for C–C bond cleavage, thereby favoring ethanol dehydrogenation to acetaldehyde. Additionally, the reduced surface area limits available oxygen-vacancy sites and steam adsorption in the matrix surface, both critical for carbon gasification. Aside from dehydrogenation, ethanol may undergo the same reaction pathways observed for the LSTN 650 sample, although with distinct relative contributions due to the modification of the materials surface.

The LSTN 1200 sample (Fig. 5c) demonstrates severely diminished ethanol conversion and intensified dehydrogenation, consistent with its low surface area. This behavior was previously documented for high-temperature-calcined catalysts [20]. The LSTN 1200 sample yielded only ~8 % ethanol conversion, with acetaldehyde as the dominant product (>90 %) via the pathway described in Equation (8).

While exsolved Ni^0 NPs are present in all catalysts, as clearly evidenced by FE-SEM and XRD analyses, catalytic performance is governed by specific surface area and Ni^0 nanoparticle characteristics. As the calcination temperature increases, the surface area declines sharply. The surface area decrease drives a corresponding drop in ethanol conversion from 100 % (LSTN 650) to 68 % (LSTN 800) and finally to ~8 % (LSTN 1200), with dehydrogenation to acetaldehyde becoming increasingly favored. An intrinsic driving force for particle segregation is the surface free energy, which scales with the material's surface area [35]. Consequently, the loss of surface area can induce the exsolution of larger, coke-susceptible Ni^0 NPs. The carbon deposits then block the active metallic NPs required for C–C cleavage, suppressing reforming pathways. Furthermore, reduced surface-active sites, oxygen vacancies and compromised steam activation hinder the gasification of newly formed carbon, accelerating the overall deactivation process.

Owing to its enhanced hydrogen production performance, the LSTN 650 catalyst was subjected to an 85-h stability test at 500 °C. This temperature was selected specifically to probe deactivation behavior, given that complete ethanol conversion was previously achieved at 600 °C. As depicted in Fig. 6, significant deactivation occurred within the first 15 h, probably due to coke accumulation, with ethanol conversion declining from 100 % to ~40 %, where it subsequently stabilized.

Product distribution analysis revealed sustained formation of H_2 (~48 %), acetaldehyde (31 %), CO and CO_2 (10 % each), and CH_4 (>5 %), after the initial 15 h of the reaction. This profile indicates competing reaction pathways analogous to LSTN 800 at 600 °C, though the elevated CO_2 production confirms greater WGS contribution for LSTN 650 at 500 °C. Notably, the stabilized hydrogen yield reached 1.10 mol mol $^{-1}_{ethanol}$, achieving consistent long-term hydrogen production capacity despite partial deactivation.

Calculations of the carbon balance and carbon-based selectivities, derived from the product distribution and feed flow, are provided in Supplementary Table S3. These data corroborate the coexistence of reforming and dehydrogenation pathways and show that the carbon balance closes to ≈100 % for all samples, supporting the consistency of the experiments.

Confirmation of carbon deposition on the sample surfaces is provided by Raman spectra in Fig. 7a. Carbon species are typically identified by the presence of the D and G bands. The G band (~1600 cm^{-1}) originates from the fundamental in-plane vibration of carbon atoms in ordered graphitic lattices. The D band (1300–1400 cm^{-1}) is defect-activated, requiring both an in-plane transverse optical (iTO) phonon vibration and structural defects within the carbon lattice. Its intensity correlates directly with defect density [36–38]. All samples presented both D and G bands.

Thermogravimetric (TG) analysis of the spent catalyst shows that the

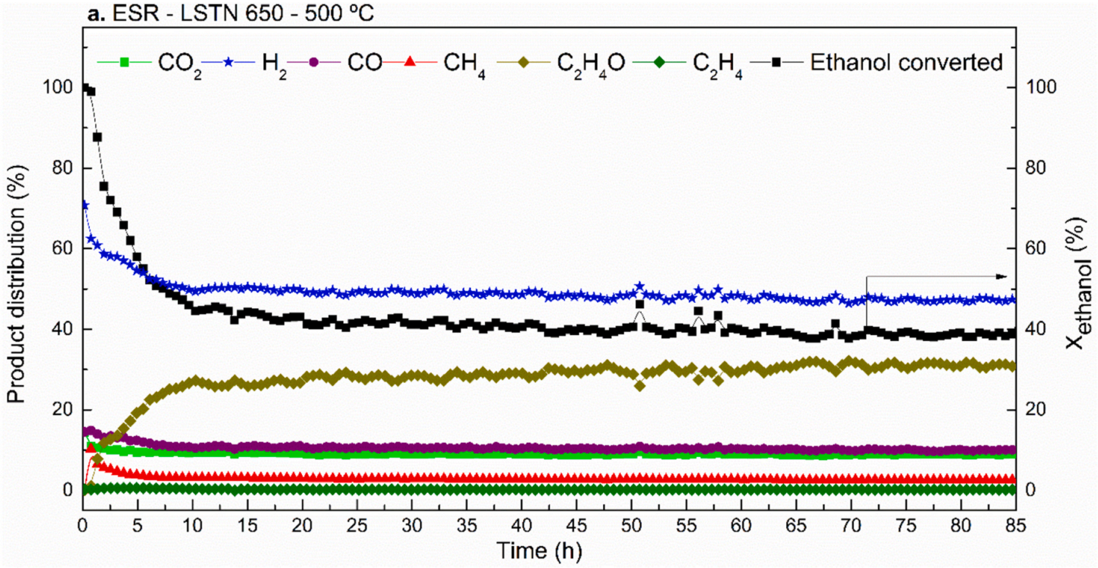

Fig. 6. Ethanol conversion ($X_{ethanol}$) and product distributions during ESR tests over the LSTN 650, sample at 500 °C for 85 h (Catalyst mass = 20 mg; W/F = 0.020 g s mL^{-1}).

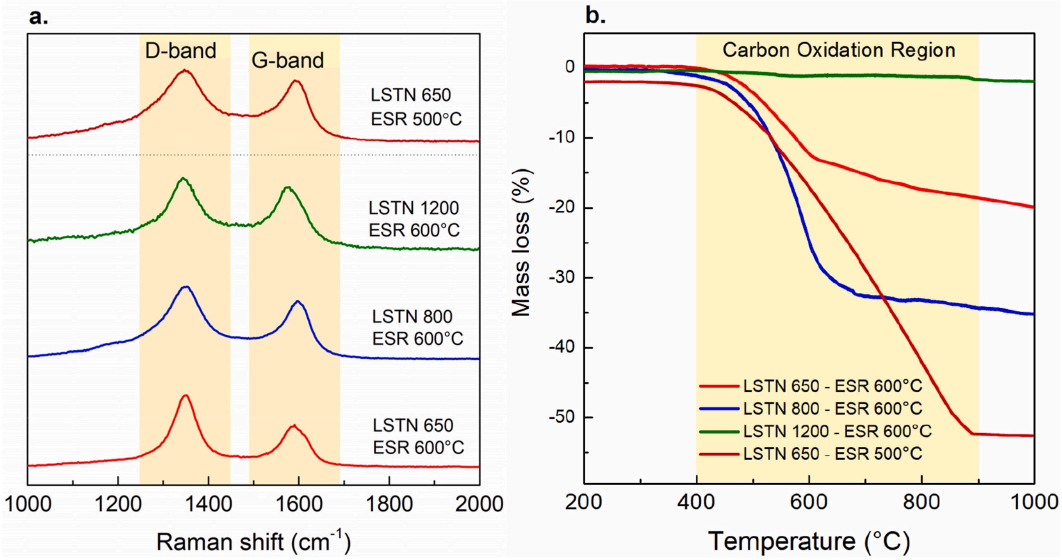

Fig. 7. – (a) Raman spectra and (b) thermogravimetric analysis of the spent catalysts after ESR reaction: all samples tested at 600 °C and the LSTN 650 sample at 500 °C (stability test).

nature of the deposited carbon depends strongly on testing conditions and time-on-stream. Mass-loss profiles within the carbon oxidation temperature window reveal distinct oxidation behaviors. The LST1200 shows no significant mass loss event, compatible with low ethanol conversion and the dehydrogenation pathway observed in the catalytic test. The LSTN 800 has a single mass loss event in a well-defined temperature range, from the onset at ~400 °C to ~700 °C, characteristic of highly reactive, disordered carbon. The LSTN 650 samples for both tests at 500 °C and 600 °C exhibit a similar onset, but a more extended mass loss profile, indicating a fraction of ordered, graphitic carbon. Such a behavior of the LSTN650 is significantly more pronounced for the sample tested for longer reaction time at 500 °C in which mass loss developed up to 900 °C.

TG quantification (Table 1) connects these trends to catalyst performance and operating conditions. LSTN 1200 displays the lowest carbon formation rate (0.42 $mg_C \cdot g_{cat}^{-1} \cdot h^{-1}$), likely due to its low ethanol conversion, which suppresses secondary carbon-forming pathways. Among the active materials, LSTN 650 accumulates far less carbon than LSTN 800 (7.37 vs. 25.22 $mg_C \cdot g_{cat}^{-1} \cdot h^{-1}$), consistent with the superior catalytic activity of LSTN 650. During the 85 h stability test at 500 °C, the average carbon deposition on LSTN 650 increased to 13.30 $mg_C \cdot g_{cat}^{-1} \cdot h^{-1}$. Notably, TG data evidence that this carbon is more graphitic, suggesting it may be less encapsulating than amorphous deposits and therefore less detrimental to long-term activity [39].

The catalytic performance of LSTN 650 is consistent with reports that redox-active Ni-based catalysts favor reforming pathways and enhanced H_2 production. For instance, ceria redox behavior modulate H_2 yield and coke resistance [6,40,41], whereas Ni–Al_2O_3 supports generally require promoter engineering to sustain ESR activity and hydrogen productivity [42]. Therefore, under comparable ESR conditions, LSTN 650 catalysts are more likely to reproduce the high conversion and H_2-rich selectivity observed for redox-active catalysts.

4. Conclusion

This study demonstrates that the calcination temperature of $La_{0.4}Sr_{0.4}Ti_{0.8}Ni_{0.2}O_{3-\delta}$ (LSTN) perovskite is a determinant parameter of the morphology, reducibility, and ultimately, catalytic performance in ethanol steam reforming for hydrogen production. Low calcination temperatures (650 °C) preserved a high specific surface area of the perovskite that facilitated nickel reduction at relatively low temperatures (bulk Ni reduction at 503 °C) and enabled the exsolution of Ni^0 NPs (5–15 nm) upon reduction. Catalytic testing at 600 °C revealed that LSTN calcined at 650 °C (LSTN 650) and reduced at 900 °C achieved complete and stable ethanol conversion with a high H_2 yield of 4.04 mol $mol_{ethanol}^{-1}$ and negligible coke formation. In contrast, increasing calcination temperature to 800 °C and 1200 °C resulted in significantly decreased surface area of the parent oxide, which hindered reducibility. This decrease in surface area limits the formation of accessible Ni^0 sites and shifts the reaction pathway toward ethanol dehydrogenation and acetaldehyde formation.

Calcination temperature functions as a practical parameter because it directly affects surface area, nickel reducibility and exsolution. These parameters have a direct relation to the catalyst performance. A high initial surface area provides more accessible Ni^0 sites and promotes favorable nanoparticle characteristics that sustain the ESR pathway. When surface area decreases, larger Ni particles form and become more susceptible to carbon deposition. Therefore, maintaining a high surface area is essential to maximize the availability of active sites, enable efficient H_2 production, suppress undesirable side reactions, and minimize carbon accumulation. The robustness of the studied catalyst was evaluated in an extended 85-h stability test in which despite the partial deactivation it maintained a consistent H_2 yield, confirming good long-term stability at harsh conditions (500 °C).

These findings highlight a simple route to tune exsolution-derived catalysts through calcination control and Ni-doped LST perovskites as promising non-noble catalyst for renewable hydrogen production from bioethanol.

CRediT authorship contribution statement

Fernando Piazzolla: Writing – review & editing, Writing – original draft, Validation, Investigation, Formal analysis, Conceptualization. **Emerson L. dos Santos Veiga:** Writing – review & editing, Writing – original draft, Validation, Methodology, Investigation, Formal analysis, Data curation, Conceptualization. **Rafael A. Vicente:** Writing – review & editing, Writing – original draft, Visualization, Validation, Methodology, Formal analysis, Data curation. **Wei-Ling Huang:** Validation, Methodology, Formal analysis, Data curation. **Shan Jiang:** Validation, Methodology, Formal analysis, Data curation. **Pablo S. Fernández:** Writing – review & editing, Validation, Supervision, Resources, Formal analysis. **Jeffrey T. Miller:** Writing – review & editing, Supervision, Resources, Funding acquisition, Formal analysis. **Fabio C. Fonseca:** Writing – review & editing, Validation, Supervision, Resources, Project administration, Methodology, Funding acquisition, Formal analysis, Conceptualization.

Declaration of competing interest

The authors declare that they have no known competing financial interests or personal relationships that could have appeared to influence the work reported in this paper.

Acknowledgements

Authors acknowledge the funding from Brazilian agencies CNEN; Conselho Nacional de Pesquisa Científica e Tecnológica (CNPq) grants 446879/2024-0, 314801/2025-1, and Sis-H2 407967/2022-2 (CNPq); Coordenação de Aperfeiçoamento de Pessoal de Nível Superior Brasil (CAPES) for Finance Code 001; Fundação de Amparo à Pesquisa do Estado de São Paulo (FAPESP) grants 2017/11937-4, 2018/19251-7, 2021/02678-0, 2024/00989-7, and 2023/14931-8; and Financiadora de Estudos e Projetos (FINEP) process no. 01.18.0073.00 (FINEP).

This research used resources at the 8-ID beamline of the National Synchrotron Light Source II, a U.S. Department of Energy (DOE) Office of Science User Facility operated for the DOE Office of Science by Brookhaven National Laboratory under Contract No. DE-SC0012704 (DOE). FCF is a CNPq fellow.

Appendix A. Supplementary data

Supplementary data to this article can be found online at https://doi.org/10.1016/j.ijhydene.2025.153326.

References

[1] Khan MAH, Bonifacio S, Clowes J, Foulds A, Holland R, Matthews JC, et al. Investigation of biofuel as a potential renewable energy source. Atmosphere 2021;12:1289. https://doi.org/10.3390/atmos12101289.

[2] Kabeyi MJB, Olanrewaju OA. Sustainable energy transition for renewable and low carbon grid electricity generation and supply. Front Energy Res 2022;9. https://doi.org/10.3389/fenrg.2021.743114.

[3] Marouani I, Guesmi T, Alshammari BM, Alqunun K, Alzamil A, Alturki M, et al. Integration of renewable-energy-based green hydrogen into the energy future. Processes 2023;11:2685. https://doi.org/10.3390/pr11092685.

[4] Sadik-Zada ER. Political economy of green hydrogen rollout: a global perspective. Sustainability 2021;13:13464. https://doi.org/10.3390/su132313464.

[5] Guan G, Kaewpanha M, Hao X, Abudula A. Catalytic steam reforming of biomass tar: prospects and challenges. Renew Sustain Energy Rev 2016;58:450–61. https://doi.org/10.1016/j.rser.2015.12.316.

[6] Meng H, Zhang J, Yang Y. Recent status in catalyst modification strategies for hydrogen production from ethanol steam reforming. ChemCatChem 2023;15. https://doi.org/10.1002/cctc.202300733.

[7] da Silva AAA, Steil MC, Tabuti FN, Rabelo-Neto RC, Noronha FB, Mattos LV, et al. The role of the ceria dopant on Ni/doped-ceria anodic layer cermets for direct ethanol solid oxide fuel cell. Int J Hydrogen Energy 2021;46:4309–28. https://doi.org/10.1016/j.ijhydene.2020.10.155.

[8] Wu C, Dupont V, Nahil MA, Dou B, Chen H, Williams PT. Investigation of Ni/SiO_2 catalysts prepared at different conditions for hydrogen production from ethanol steam reforming. J Energy Inst 2017;90:276–84. https://doi.org/10.1016/j.joei.2016.01.002.

[9] Phung TK, Pham TLM, Nguyen A-NT, Vu KB, Giang HN, Nguyen T-A, et al. Effect of supports and promoters on the performance of ni-based catalysts in ethanol steam reforming. Chem Eng Technol 2020;43:672–88. https://doi.org/10.1002/ceat.201900445.

[10] Carvalho SGM, Tabuti FN, Santiago EI, Abe R, Guimarães RM, Miura Y, et al. Advancing direct ethanol metal supported fuel cells with catalytic layer. Mater Sci Eng, B 2025;318:118259. https://doi.org/10.1016/j.mseb.2025.118259.

[11] Kim YH, Jeong H, Won B-R, Jeon H, Park C, Park D, et al. Nanoparticle exsolution on perovskite oxides: insights into mechanism, characteristics and novel strategies. Nano-Micro Lett 2024;16:33. https://doi.org/10.1007/s40820-023-01258-4.

[12] Moraes TS, Tinti VB, de Florio DZ, Ferlauto AS, Piazzolla F, Miura Y, et al. Enhanced ethanol reforming with catalytic active ruthenium species derived from solid solution in lanthanum chromite. Catal Sci Technol 2025;15:5907–23. https://doi.org/10.1039/D5CY00774G.

[13] O'Leary W, Giordano L, Park J, Nonnenmann SS, Shao-Horn Y, Rupp JLM. Influence of Sr-Site deficiency, Ca/Ba/La doping on the exsolution of Ni from $SrTiO_3$. J Am Chem Soc 2023;145:13768–79. https://doi.org/10.1021/jacs.2c12011.

[14] Rudolph B, Tsiotsias AI, Ehrhardt B, Dolcet P, Gross S, Haas S, et al. Nanoparticle exsolution from nanoporous perovskites for highly active and stable catalysts. Adv Sci 2023;10. https://doi.org/10.1002/advs.202205890.

[15] Lindenthal L, Rameshan R, Summerer H, Ruh T, Popovic J, Nenning A, et al. Modifying the surface structure of perovskite-based catalysts by nanoparticle exsolution. Catalysts 2020;10:268. https://doi.org/10.3390/catal10030268.

[16] Tinti VB, Marani D, Ferlauto AS, Fonseca FC, Esposito V, de Florio DZ. Exsolution of nickel nanoparticles from mixed-valence metal oxides: a quantitative evaluation by magnetic measurements. Part Part Syst Char 2020;37. https://doi.org/10.1002/ppsc.201900472.

[17] Neagu D, Tsekouras G, Miller DN, Ménard H, Irvine JTS. In situ growth of nanoparticles through control of non-stoichiometry. Nat Chem 2013;5:916–23. https://doi.org/10.1038/nchem.1773.

[18] Sun X, Chen H, Yin Y, Curnan MT, Han JW, Chen Y, et al. Progress of exsolved metal nanoparticles on oxides as high performance (Electro)Catalysts for the conversion of small molecules. Small 2021;17. https://doi.org/10.1002/smll.202005383.

[19] Zhang J, Gao M-R, Luo J-L. In situ exsolved metal nanoparticles: a smart approach for optimization of catalysts. Chem Mater 2020;32:5424–41. https://doi.org/10.1021/acs.chemmater.0c00721.

[20] Piazzolla F, Moraes TS, Figueiredo SS, de Paula DF, dos Santos Veiga EL, Rodella CB, et al. Exsolution of Ni nanoparticles from $La_{0.4}Sr_{0.4}Ti_{0.8}Ni_{0.2}O_{3\text{-}\delta}$ perovskite for ethanol steam reforming. Catal Today 2025;444:115011. https://doi.org/10.1016/j.cattod.2024.115011.

[21] Moraes TS, Bergamaschi VS, Ferreira JC, Spinacé EV. Preparation and characterization of high-performance Ni-based core–shell catalyst for ethanol steam reforming. J Mater Sci 2022;57:5384–95. https://doi.org/10.1007/s10853-022-06969-4.

[22] Chang S, Mao W, Na W, Gao W, Qu G, Wang H. Study on the performance of NiO/Zn_xZr_{1-x} catalysts for CO_2 hydrogenation. RSC Adv 2020;10:42790–8. https://doi.org/10.1039/D0RA07660K.

[23] Vera E, Trillaud V, Metaouaa J, Aouine M, Boreave A, Burel L, et al. Comparative study of exsolved and impregnated Ni nanoparticles supported on nanoporous perovskites for low-temperature CO oxidation. ACS Appl Mater Interfaces 2024;16:7219–31. https://doi.org/10.1021/acsami.3c17300.

[24] Angel RJ, Bismayer U, Marshall WG. Local and long-range order in ferroelastic lead phosphate at high pressure. Acta Crystallogr B 2004;60:1–9. https://doi.org/10.1107/S0108768103026582.

[25] dos Santos Veiga EL, Díaz-Verde Á, Illán-Gómez MJ, Beltrán-Mir H, Cordoncillo E. Evaluation of $Pr_2Zr_{2-x}Ce_xO_{7\pm\delta}$ pyrochlores as a potential Cu support catalysts for CO oxidation in simulated GDI conditions. Appl Catal, B 2024;342:123371. https://doi.org/10.1016/j.apcatb.2023.123371.

[26] Neagu D, Oh T-S, Miller DN, Ménard H, Bukhari SM, Gamble SR, et al. Nano-socketed nickel particles with enhanced coking resistance grown in situ by redox exsolution. Nat Commun 2015;6:8120. https://doi.org/10.1038/ncomms9120.

[27] Zhang G, Yang C, Miller JT. Tetrahedral Nickel(II) phosphosilicate single-site selective propane dehydrogenation catalyst. ChemCatChem 2018;10:961–4. https://doi.org/10.1002/cctc.201701815.

[28] Okere CJ, Sheng JJ. Review on clean hydrogen generation from petroleum reservoirs: fundamentals, mechanisms, and field applications. Int J Hydrogen Energy 2023;48:38188–222. https://doi.org/10.1016/j.ijhydene.2023.06.135.

[29] Ratnasamy C, Wagner JP. Water gas shift catalysis. Catal Rev 2009;51:325–440. https://doi.org/10.1080/01614940903048661.

[30] Winkler CA, Hinshelwood CN. The thermal decomposition of acetaldehyde. Proc R Soc Lond A Math Phys Sci 1935;149:355–9. https://doi.org/10.1098/rspa.1935.0067.

[31] Sivaramakrishnan R, Michael JV, Harding LB, Klippenstein SJ. Resolving some paradoxes in the thermal decomposition mechanism of acetaldehyde. J Phys Chem A 2015;119:7724–33. https://doi.org/10.1021/acs.jpca.5b01032.

[32] Yasunaga K, Kubo S, Hoshikawa H, Kamesawa T, Hidaka Y. Shock-tube and modeling study of acetaldehyde pyrolysis and oxidation. Int J Chem Kinet 2008;40:73–102. https://doi.org/10.1002/kin.20294.

[33] Ogo S, Sekine Y. Recent progress in ethanol steam reforming using non-noble transition metal catalysts: a review. Fuel Process Technol 2020;199:106238. https://doi.org/10.1016/j.fuproc.2019.106238.

[34] Zhang X, Zhang L, Peng H, You X, Peng C, Xu X, et al. Nickel nanoparticles embedded in mesopores of AlSBA-15 with a perfect peasecod-like structure: a catalyst with superior sintering resistance and hydrothermal stability for methane dry reforming. Appl Catal, B 2018;224:488–99. https://doi.org/10.1016/j.apcatb.2017.11.001.

[35] Hu F, Wei B, He B, Yu X, Zhao S, Chen Y, et al. Recent advances and future prospects in exsolution technology for solid oxide cells. Energy Rev 2025;4:100141. https://doi.org/10.1016/j.enrev.2025.100141.

[36] Ferrari AC, Basko DM. Raman spectroscopy as a versatile tool for studying the properties of graphene. Nat Nanotechnol 2013;8:235–46. https://doi.org/10.1038/nnano.2013.46.

[37] Tan PH, Han WP, Zhao WJ, Wu ZH, Chang K, Wang H, et al. The shear mode of multilayer graphene. Nat Mater 2012;11:294–300. https://doi.org/10.1038/nmat3245.

[38] Li Z, Deng L, Kinloch IA, Young RJ. Raman spectroscopy of carbon materials and their composites: Graphene, nanotubes and fibres. Prog Mater Sci 2023;135:101089. https://doi.org/10.1016/j.pmatsci.2023.101089.

[39] Mo W-L, Ren Y, Ma Y, Guo J, Feng Z-H, Zhang S-P, et al. Structure characteristics and removal behavior of the deposited carbon on Ni-Al_2O_3 catalyst for CO_2 reforming of CH4. Processes 2023;11:2968. https://doi.org/10.3390/pr11102968.

[40] Bao T, zhou H, Zhang Y, Guo C, Guo W, Qin H, et al. Effect of CeO_2 on carbon deposition resistance of Ni/CeO_2 catalyst supported on SiC porous ceramic for ethanol steam reforming. J Rare Earths 2023;41:1703–13. https://doi.org/10.1016/j.jre.2022.09.006.

[41] Balopi B, Joshua G, Moyo M, Liu X. Dry reforming of model-biogas over ceria-supported nickel catalyst: the effect of charge enhanced dry impregnation on the catalytic performance and coke resistance. Res Chem Intermed 2024;50:4175–98. https://doi.org/10.1007/s11164-024-05362-x.

[42] Shi K, An X, Du Y, Fan Z, Wu X, Xie X. Improving the coking resistance of Ni/Al_2O_3 modified by promoter (Ce, Zr, or Mg) under ethanol steam reforming: perspective from growth sites of coking. J Energy Inst 2022;104:35–45. https://doi.org/10.1016/j.joei.2022.07.003.